Nanostructures

DOI: 10.1002/anie.201410154

Compact Coupled Graphene and Porous Polyaryltriazine-Derived Frameworks as High Performance Cathodes for Lithium-Ion Batteries**

Yuezeng Su, Yuxin Liu, Ping Liu, Dongqing Wu, Xiaodong Zhuang, Fan Zhang, and Xinliang Feng**

Abstract: *It is highly desirable to develop electroactive organic materials and their derivatives as green alternatives of cathodes for sustainable and cost-effective lithium-ion batteries (LIBs) in energy storage fields. Herein, compact two-dimensional coupled graphene and porous polyaryltriazine-derived frameworks with tailormade pore structures are fabricated by using various molecular building blocks under ionothermal conditions. The porous nanosheets display nanoscale thickness, high specific surface area, and strong coupling of electroactive polyaryltriazine-derived frameworks with graphene. All these features make it possible to efficiently depress the dissolution of redox moieties in electrolytes and to boost the electrical conductivity of whole electrode. When employed as a cathode in LIBs, the two-dimensional porous nanosheets exhibit outstanding cycle stability of 395 mAh g^{-1} at 5 A g^{-1} for more than 5100 cycles and excellent rate capability of 135 mAh g^{-1} at a high current density of 15 A g^{-1}.*

It is a timely observation to state that clean and efficient energy storage systems should be established to cope with the increasing energy demand in the near future. The development of state-of-the-art lithium-ion batteries (LIBs) has reached a bottleneck. Part of the reason is that present LIBs for portable electronics are based on inorganic intercalation cathode materials, which have drawbacks including limited mineral resources, low theoretical capacities, and relatively high costs.[1] Electroactive organics and their derivatives represent an emerging and promising alternative as cathodes for sustainable and cost-effective LIBs.[2] More importantly, through molecular-level design, the morphological and electrochemical properties of the target compounds are predictably tuned towards high-performance cathode materials with multielectron reactions.[3] Although extensive efforts have been devoted to these cathodes, such as using carbonyl compounds, organosulfur compounds, radical polymers, conducting polymers etc.,[3c,4a] the most severe problems are associated with the relatively poor electrical conductivity and high solubility of redox-active organic moieties in electrolytes,[2a,b,3c,4] which are detrimental to the high-rate capability and long-term cyclability. Therefore, there is an urgent demand for designing and constructing cathodes with a high energy density and long cycle life for the next-generation LIBs.

The judiciously designed two-dimensional (2D) graphene-based porous nanohybrids possess large aspect ratios, well-defined pore structures, high surface areas, and excellent electrical conductivity,[5] which demonstrate appeal as electrode materials in LIBs. Herein we present an unprecedented protocol for the fabrication of compact 2D coupled graphene-porous polyaryltriazine-derived frameworks (G-PPFs) in which electroactive aromatic networks with tailor-made pore structures are immobilized on the graphene substrate through covalent bonding. The resulting strong coupling of electroactive aromatic frameworks with graphene efficiently depresses the dissolution of active moieties in electrolytes. Given the benefits of intentional adjustment of various molecular building blocks and different temperatures for the synthesis, tuning of the pore sizes from 2.1 to 7.3 nm and the specific surface areas from 651 to 1683 $m^2 g^{-1}$ can be achieved. Serving as a cathode for LIBs, the tightly coupled 2D nanohybrids exhibit an outstanding cycle stability of 395 mAh g^{-1} at 5 A g^{-1} for more than 5100 cycles and excellent rate capability of 135 mAh g^{-1} at a high current density of 15 A g^{-1}. With its extremely long cycle life and high charge-discharge rates, the superior performance of the 2D porous nanosheets undoubtedly goes far beyond the previously reported cathode materials (see Table S1 in the Supporting Information).

[*] Prof. Y. Su[+]
School of Electronic Information and Electrical Engineering, Shanghai Jiao Tong University (P.R. China)
Y. Liu[+]
School of Aeronautics and Astronautics, Shanghai Jiao Tong University (P.R. China)
Dr. P. Liu, Dr. D. Wu, Dr. X. Zhuang, Prof. F. Zhang, Prof. X. Feng
School of Chemistry and Chemical Engineering
Shanghai Jiao Tong University
600 Dongchuan RD, Shanghai 200240 (P.R. China)
E-mail: liupingsjj@sjtu.edu.cn
Prof. X. Feng
Technische Universitaet Dresden
01062 Dresden (Germany)
E-mail: xinliang.feng@tu-dresden.de
[+] These authors contributed equally to this work.

[**] This work was financially supported by the 973 Program of China (2012CB933404, 2013CBA01602, and 2014CB239701), Natural Science Foundation of China (61235007, 21174083, 21320102006, 21102091, and 21372155), Ph.D. Programs Foundation of Ministry of Education of China for Young Scholars (20110073120039), Program for Professor of Special Appointment (Eastern Scholar), and ERC 2DMATER. We also thank the Instrumental Analysis Center of Shanghai Jiao Tong University for provide some measurements.
Supporting information for this article is available on the WWW under http://dx.doi.org/10.1002/anie.201410154.

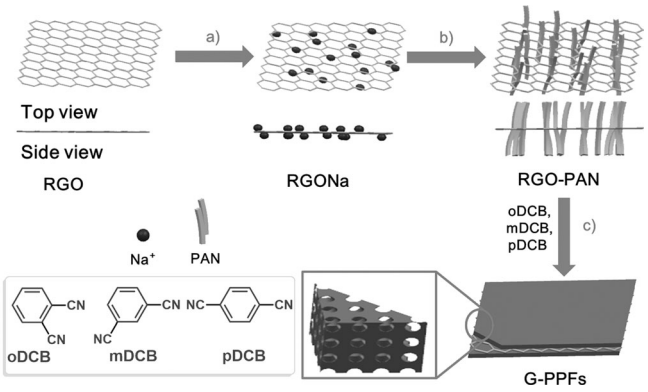

Scheme 1. Compact coupled graphene and porous polyaryltriazine-derived frameworks. a) The formation of graphene-based 2D carbanions. b) Anionic polymerization of acrylonitrile on the surface of RGO. c) The trimerization of 1,4-dicyanobenzene (pDCB), 1,3-dicyanobenzene (mDCB), and 1,2-dicyanobenzene (oDCB) in the presence of RGO-PAN at 400 °C for 40 h, 600 °C for 20 h, or 400 °C for 20 h then 600 °C for 20 h in $ZnCl_2$ (vacuum).

The strategy for the synthesis of G-PPFs is depicted in Scheme 1. Dynamic trimerization of aromatic polynitriles has guaranteed the syntheses of porous crystalline or amorphous covalent triazine frameworks (generally abbreviated as CTFs in previous reports).[6] Inspired by this fact, a series of G-PPFs with controllable porosities have been deliberately designed by employing the polyacrylonitrile-functionalized graphene nanosheet[7] (RGO-PAN) as a template. Briefly, the graphene-based 2D carbanions (RGONa) were created by direct reaction between sodium and reduced graphene oxide (RGO) in anhydrous tetrahydrofuran (THF) with the aid of ultrasonic treatment. Next, the graphene-based carbanions were used as initiators for the anionic polymerization of acrylonitrile on the graphene surfaces, thus affording RGO-PAN as a black powder. Finally, to access tailormade pore structures, the controlled polymerization of diverse molecular building blocks, including 1, 4-dicyanobenzene (pDCB), 1, 3-dicyanobenzene (mDCB), and 1, 2-dicyanobenzene (oDCB), was triggered on the surface of RGO-PAN in molten $ZnCl_2$. The as-obtained G-PPFs synthesized at 300 °C for 20 hours, at 400 °C for 40 hours, at 600 °C for 20 hours, or at 400 °C for 20 hours then 600 °C for 20 hours, denoted G-PPF-p-300, G-PPF-p-400 (G-PPF-m-400, G-PPF-o-400), G-PPF-p-600, and G-PPF-p-400-600, respectively, were obtained after washing the resulting solids with 1 M HCl. For comparison, the corresponding PPFs were also synthesized without adding RGO-PAN (denoted as PPF-p-X, PPF-m-X, and PPF-o-X, where X represents reaction temperature). Additionally, pure RGO-PAN, without adding aromatic nitriles, was treatedin molten $ZnCl_2$ at 300, 350, and 400 °C for 5 hours, and designated G-PAN-300, G-PAN-350, and G-PAN-400, respectively.

The successful build-up of G-PPFs was firstly confirmed by Fourier transform infrared (FT-IR) spectroscopy (see Figures S1 and S2). The characteristic absorption peak B (2204 cm^{-1}) of RGO-PAN can be attributed to the stretch of the nitrile bond,[7] thus indicating the successful surface functionalization of graphene with polyacrylonitrile. After being thermally treated at temperatures over the melting point of $ZnCl_2$ (293 °C), the stretches of the nitrile bonds still appear in G-PAN-300, G-PAN-350, and G-PAN-400, thus providing anchors for the nucleation of the triazine-based frameworks on the graphene surface through covalent bonding. The characteristic absorption peaks A (at 1352 and 1556 cm^{-1}) can be assigned to the presence of the triazine rings[5a,6a] in the FT-IR spectra of G-PPF-p-300, PPF-p-400, G-PPF-p-400, G-PPF-p-400-600, and G-PPF-p-600, and suggest that the dynamic trimerization of aromatic nitriles takes place from 300 °C. The X-ray diffraction (XRD) patterns of both PPFs and G-PPFs (see Figure S3) exhibit the broadness of the peaks, thus suggesting that these polyaryltriazine-derived networks have amorphous features.[4f,8] Raman spectra of RGO, G-PPF-p-400, G-PPF-p-600, and G-PPF-p-400-600 (see Figure S4) exhibit two strong peaks at about 1350 and 1580 cm^{-1}, which can be attributed to the D (disordered) and G (ordered) bands of carbon,[7] respectively. The decreased I_D/I_G values of G-PPF-p-400 ($I_D/I_G = 0.92$), G-PPF-p-600 ($I_D/I_G = 1.01$), and G-PPF-p-400-600 ($I_D/I_G = 1.02$) compared with that of RGO ($I_D/I_G = 1.25$) indicate the lower defect density and the enhanced graphitic degree resulting from tightly covalent binding between polyaryltriazine-derived frameworks and graphene nanosheets.[7]

The morphology and microstructure of G-PPFs were further inspected by scanning electron microscopy (SEM), transmission electron microscopy (TEM), and atomic force microscopy (AFM). All G-PPFs display analogous sheetlike architectures (see Figure 1 a–d and Figure S6), thus inheriting the 2D morphology of the RGO-PAN template (Figure S5 a,b). This result suggests the strong coupling between graphene and PPFs, which are directed by the PAN backbone during the ionothermal reaction. The sizes of these 2D nanosheets range from hundreds of nanometers to several micrometers. As indicated by TEM images, the wrinkled surface of the nanosheets with many alternative dark and light areas (Figure 1 b,c) suggests the presence of numerous pores[5a] in G-PPF-p-400-600. The corresponding elemental mapping images support the homogeneous distribution of

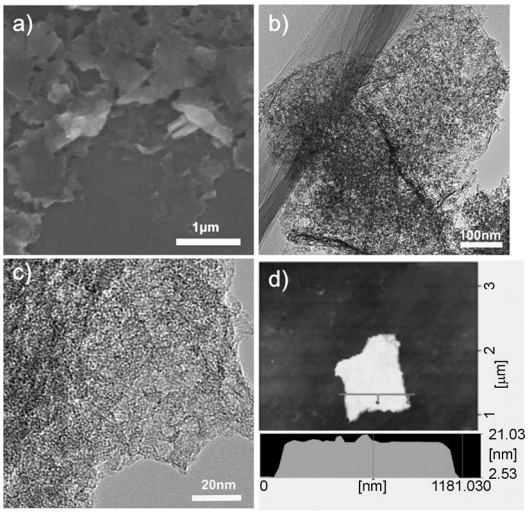

Figure 1. a) SEM, b) TEM, c) HRTEM, and d) AFM images of G-PPF-p-400-600.

nitrogen on these nanosheets (see Figure S7). High-resolution TEM (HRTEM) images (Figure 1c, and Figure S6b,d) clearly indicate the presence of additional mesopores in G-PPF-p-600 and G-PPF-p-400-600, which do not resemble that of G-PPF-p-400.[6,9a] AFM confirms the 2D morphology of the G-PPFs with a uniform thickness of about 16 nm (Figure 1d). Strongly distinct from G-PPFs, PPF-p-400 only manifests obvious aggregation and macroscopic heterogeneities (see Figure S5c,d).These results validate that the use of RGO-PAN in our approach effectively overcomes the incompatibility between the graphene nanosheets and the porous polymeric frameworks.

Consequently, nitrogen physisorption measurements were carried out to gain further insight into the porosities of the 2D porous aromatic frameworks. The type I isotherm is observed for G-PPF-o-400, whereas type IV isotherms with an associated H2-type hysteresis are exhibited for G-PPF-m-400, G-PPF-p-400, G-PPF-p-600, and G-PPF-p-400-600 (Figure 2a). All the above is indicative of the formation of mesopores in these samples except for G-PPF-o-400, and in line with HRTEM observations. The Brunauer–Emmett–Teller (BET) specific surface areas of G-PPF-o-400, G-PPF-m-400, G-PPF-p-400, G-PPF-p-600, and G-PPF-p-400-600 are calculated to be 651, 1238, 1285, 1414, and 1683 $m^2 g^{-1}$, respectively. The variation of the pore sizes is further verified by the corresponding pore-size distribution based upon density functional theory (DFT) calculations (Figure 2b). The average pore sizes (D_{Av}) of G-PPF-o-400, G-PPF-m-400, G-PPF-p-400, G-PPF-p-400-600, and G-PPF-p-600 are about 2.1, 2.5, 2.9, 3.7, and 7.3 nm, respectively, which also demonstrate the creation of mesoporous structure (see Figure 2c and Table S2). The formation of continuous porous frameworks might be disrupted by the increased steric hindrance from two neighboring nitrile groups in *o*-DCB, and thus results in a significantly decreased specific surface area for G-PPF-o-400. In contrast, G-PPF-p-400 has the largest specific surface area and average pore size compared to those of G-PPF-o-400 and G-PPF-m-400, thus suggesting that the reduced steric effect in the monomer of *p*-DCB facilitates the formation of continuous networks. Moreover, with the increase of reaction temperature from 400 °C to 600 °C, the number of additional mesopores grows, which leads to the remarkable increase in specific surface area[9a,6c–d] in the corresponding samples, especially for G-PPF-p-400-600 through consecutive reactions.[6c–d] By taking advantage of the 2D feature of graphene nanosheets,[5a] all G-PPFs have higher specific surface areas than the corresponding PPFs which do not contain graphene (see Figure S8 and Table S2).

The chemical compositions of G-PPF-p-300, G-PPF-p-400, G-PPF-p-600, G-PPF-p-400-600 together with RGO-PAN and G-PAN-300 were further probed by X-ray photoelectron spectroscopy (XPS). The N1s spectra of both RGO-PAN and G-PAN-300 only show one peak (398.1 eV) which is assigned to the nitrile groups from the PAN chains[9b] (see Figure S9). For G-PPF-p-300 with added aromatic nitriles in the synthetic procedure, the peak of the pyridine N in N1s spectra points to the formation of triazine rings (see Figure S10), which is in good agreement with FT-IR analysis results. The above characterizations unambiguously confirm the availability of adequate cyano groups on the graphene surface during the nucleation processes of polyaryltriazine-derived frameworks. The N1s spectra of G-PPF-p-400, G-PPF-p-600, and G-PPF-p-400-600 (see Figures S11a–c) display four N configurations: pyridine N (398.3 eV, N1), pyrrole N (400.1 eV, N2), quaternary N (401.1 eV, N3), and pyridine-*N*-oxide (403.1 eV, N4).[9a,c] On going from 400 to 600 °C, the percentages of N1 and N4 remain almost constant, whereas N2 tends to decrease and N3 increases significantly. That is, the percentages of the four N configurations vary with reaction temperatures (Figure 2d), which demonstrate the molecular-level structural transformation. The atomic percentage of nitrogen derived from XPS analysis for G-PPF-p-400, G-PPF-p-600, and G-PPF-p-400-600 is 9.1, 7.7, and 6.6%, respectively, and is in close agreement with the elemental analysis results (see Figure S11d). The depletion of nitrogen can be presumably attributed to some rearrangement and decomposition reactions of the aromatic frameworks at relatively higher temperatures.[6]

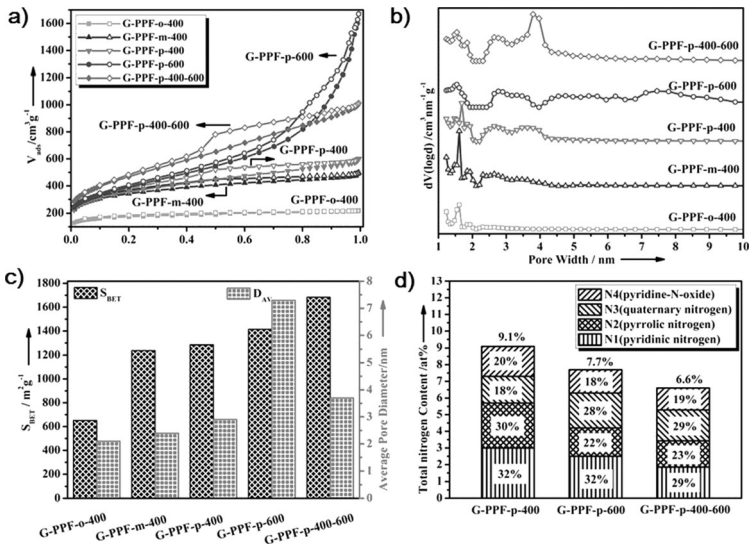

Figure 2. a) Nitrogen adsorption/desorption isotherms of G-PPFs. b) The pore-size distribution calculated by the density functional theory (DFT). c) BET surface area values and average pore sizes of G-PPFs. d) Atomic percentages of four nitrogen species for G-PPF-p-400, G-PPF-p-600, and G-PPF-p-400-600 derived from XPS analysis.

To explore the electrochemical behavior of G-PPFs as cathodes for LIBs, the cyclic voltammogram (CV) of G-PPF-p-400–600 was subsequently measured at a scan rate of 10 $mV s^{-1}$ below and above the open-circuit voltage of 3 V versus Li/Li^+ (Figure 3a), thus suggesting that the electrode had either reversible p-type (an oxidized state above 3 V versus Li/Li^+) or n-type (a reduced state below 3 V versus Li/Li^+) redox activity. Thus a large working potential window (1.5–4.5 V versus Li/Li^+) was achieved, thereby increasing the energy density by yielding a high specific capacity, as shown in the typical profiles of voltage versus specific capacity (see Figure S12a). On the basis of the previously

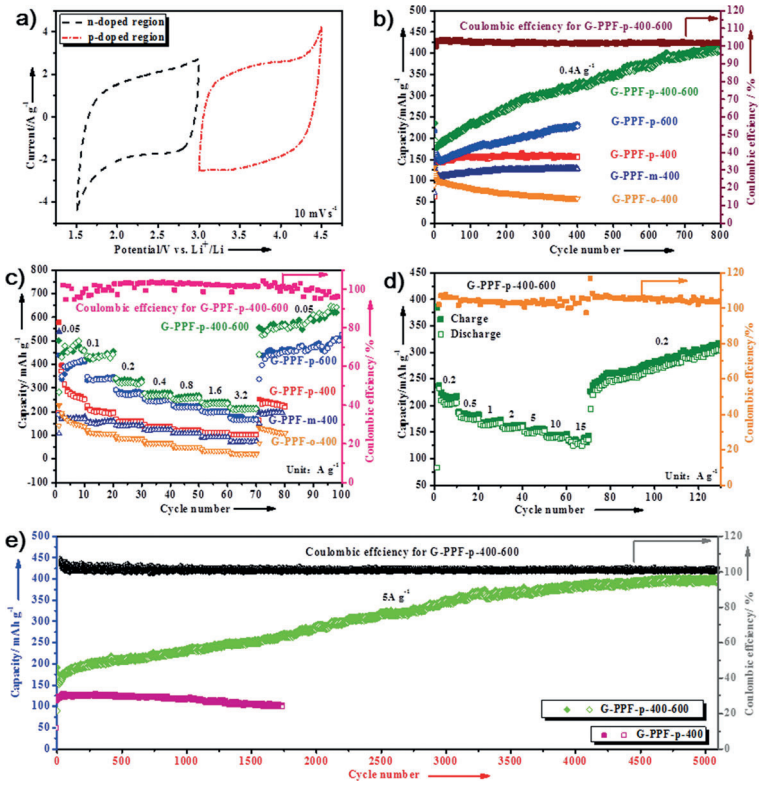

Figure 3. a) Cyclic voltammogram for G-PPF-p-400-600 electrode obtained above and below the open-circuit voltage (3 V vs. Li/Li^+). b) Cycle performance of G-PPFs electrodes at a current rate of 0.4 $A g^{-1}$ in the voltage range of 1.5–4.5 V vs. Li^+/Li. c) Rate performance of G-PPFs electrodes at various current densities in the range of 0.05–3.2 $A g^{-1}$ in the voltage range of 1.5–4.5 V vs. Li^+/Li. d) Rate performance of G-PPF-p-400-600 electrode at various current densities in the range of 0.2–15 $A g^{-1}$ in the voltage range of 1.5–4.5 V vs. Li^+/Li. e) Cycle performance of G-PPF-p-400-600 electrode (up to 5100 cycles) and G-PPF-p-400 electrode (up to 1600 cycles) at a current density of 5.0 $A g^{-1}$.

proposed energy storage mechanism for amorphous covalent triazine-based frameworks (ACTF-1) or polyparaphenylene (PPP) polymers, etc.,[4f,8c,10] the energy storage principle of G-PPFs is related to the reversible redox reaction accompanied by the association and disassociation of Li^+ (n-doped region, 1.5–3 V versus Li/Li^+) or the electrolyte anions (PF_6^-; *p*-doped region, 3-4.5 V versus Li/Li^+), wherein G-PPFs take up or give off ions to maintain electroneutrality during their oxidation and reduction. Thus, we envision that these newly prepared G-PPFs hold immense promise as novel cathode materials for LIBs.

In the galvanostatic discharge-charge measurements at a current density of 0.4 $A g^{-1}$(Figure 3b), the G-PPF-p-400-600 electrode delivers an high reversible capacity of 410 $mAh g^{-1}$ after 800 cycles. On the contrary, other G-PPFs electrodes show inferior cycling performance, even capacity decrease is observed for G-PPF-o-400 upon cycling. The capacities decrease to 225, 155, 125, and 55 $mAh g^{-1}$ for G-PPF-p-600, G-PPF-p-400, G-PPF-m-400, and G-PPF-o-400, respectively, after 400 cycles. In addition to the excellent cycle stability, the G-PPF-p-400-600 electrode also manifests favorable rate capability (Figure 3c), thus yielding capacities of 460, 260, and 230 $mAh g^{-1}$ at current densities of 0.05, 0.8, and 3.2 $A g^{-1}$, respectively. Notably, a large capacity of 500 $mAh g^{-1}$ for G-PPF-p-400-600 electrode is restored when the current density returns to 0.05 $A g^{-1}$, which is even gradually increased to 600 $mAh g^{-1}$ with nearly 100% Coulombic efficiency. These results are in sharp contrast to those of G-PPF-o-400, G-PPF-m-400, G-PPF-p-400, and G-PPF-p-600, which show continuous capacity decrease during the 10 cycles at each current density and the decay to 25, 75, 100, and 165 $mAh g^{-1}$, respectively, at a high current density of 3.2 $A g^{-1}$. Worse still, PPFs show lackluster electrochemical performance compared with G-PPFs, and demonstrates that electrochemical performance of the resultant materials can be enhanced by strong binding between electroactive amorphous polymeric frameworks and graphene nanosheets (see Figure S13).

Note that both cycle performance and rate capability of the G-PPF-p-400-600 electrode are superior to those of its counterparts, and is consistent with the results in CV (see Figure S12b). Even under rather harsh reaction conditions (10 cycles per increased current densities from 0.2 to 15 $A g^{-1}$), the G-PPF-p-400-600 electrode manifests a satisfying capacity of 135 $mAh g^{-1}$ at 15 $A g^{-1}$ within about 0.5 minutes, and it restores to about 300 $mAh g^{-1}$ at 0.2 $A g^{-1}$ after 130 cycles (Figure 3d). Even more excitingly, the G-PPF-p-400-600 electrode can be operated up to 5100 cycles with a reversible capacity of 395 $mAh g^{-1}$ at a remarkably high current density of 5 $A g^{-1}$ (Figure 3e), and the upward trend of the capacity seems to be maintained. The dramatic rise in capacity can be due in part to the reversible formation and decomposition process of an organic polymeric/gel-like film on the interface of electrode materials, as it provides interfacial storage sites for excess Li^+ through the "pseudocapacitance-type behavior".[11] Meanwhile, the gradual penetration of electrolyte into the porous structure promotes the activation of electrode materials, as well as Li^+ conduction,[11b–c,12a] which may also contribute to the gradual rise in enhanced capacity. The outstanding electrochemical performance of the G-PPF-p-400-600 electrode surpasses the previously reported redox-active polymeric cathodes, nanohybrids composed of active organics/conductive carbonaceous materials, and other graphene-based polymer nanocomposites,[2b,4d,f,12] thus highlighting the great potential of our approach in fabricating compact 2D coupled graphene-porous polyaryltriazine-derived frameworks with tailor-made porosities and properties in energy devices.

There are several factors which contribute to the superior cycle stability and rate capability of G-PPF-p-400-600. First, its nanoscale dimension in thickness allows contact at a molecular level between electroactive materials and the inner graphene conductive substrate, which is beneficial for efficient electron and ion transport. Thus a sharp increase in electrical conductivity can be expected, and this assumption has been proven by electrochemical impedance spectra. According to the equivalent circuit (see Figure S14), G-

PPF-p-400-600 possesses more depressed semicircle, as well as lower contact resistance ($R_f = 11.79\ \Omega$) and charge-transfer resistance ($R_{ct} = 0.11\ \Omega$) than its counterparts (see Table S3). Second, the consecutive rearrangement reaction associated with a molecular-level structural transformation endows G-PPF-p-400-600 with the highest specific surface area. The high specific surface area ensures good contact between electrode and electrolyte, and may also promote fast charge and discharge with high cyclability. Third, redox-active porous frameworks are strongly coupled to the surface of graphene through covalent bonding without disrupting their electroactive properties, and is evidenced by the well-maintained sheetlike morphology with uniform porous networks after cycling (see Figure S15). This feature makes it possible for the porous 2D sandwich-like nanosheets to achieve long cycle life by efficiently inhibiting the dissolution of redox moieties in electrolytes.

In summary, artificial 2D coupled graphene and porous polyaryltriazine-derived frameworks were successfully developed into affordable cathodes for rechargeable LIBs with high energy density and long cycle life. It is anticipated that this protocol for the fabrication of such porous nanohybrids, which integrate with distinctive features of a 2D sandwich-like architecture, high specific surface area, and molecular-level controlled electroactive porous frameworks, will pave the way for the ongoing research in energy-related applications.

Experimental Section

Preparation of polyacrylonitrile functionalized graphene nanosheets (RGO-PAN): The synthetic route of RGO-PAN was similar to that of our previously reported PAN-gRGO.[7] Please see more details in the Supporting Information.

Synthesis of G-PPFs, PPFs and G-PAN: The typical synthetic strategy for G-PPFs involved the employment of RGO-PAN as template and the trimerization of diverse nitrile monomers in the presence of RGO-PAN under ionothermal conditions. For comparison, PPFs and G-PAN were also fabricated by following the same synthetic procedure for G-PPFs, but in the absence of RGO-PAN and nitrile monomers, respectively. The details are available in the Supporting Information.

Received: October 16, 2014
Published online: December 16, 2014

Keywords: cathode · graphene · lithium · nanostructures · nitrogen

[1] a) M. Armand, S. Grugeon, H. Vezin, S. Laruelle, P. Ribiere, P. Poizot, J. M. Tarascon, *Nat. Mater.* **2009**, *8*, 120 – 125; b) S. W. Lee, N. Yabuuchi, B. M. Gallant, S. Chen, B. S. Kim, P. T. Hammond, Y. Shao-Horn, *Nat. Nanotechnol.* **2010**, *5*, 531 – 537; c) P. G. Bruce, B. Scrosati, J. M. Tarascon, *Angew. Chem. Int. Ed.* **2008**, *47*, 2930 – 2946; *Angew. Chem.* **2008**, *120*, 2972 – 2989; d) N. S. Choi, Z. Chen, S. A. Freunberger, X. Ji, Y. K. Sun, K. Amine, G. Yushin, L. F. Nazar, J. Cho, P. G. Bruce, *Angew. Chem. Int. Ed.* **2012**, *51*, 9994 – 10024; *Angew. Chem.* **2012**, *124*, 10134 – 10166.

[2] a) K. Hernández-Burgos, G. G. Rodriguez-Calero, W. Zhou, S. E. Burkhardt, H. D. Abruna, *J. Am. Chem. Soc.* **2013**, *135*, 14532 – 14535; b) M. Lee, J. Hong, H. Kim, H. D. Lim, S. B. Cho, K. Kang, C. B. Park, *Adv. Mater.* **2014**, *26*, 2558 – 2565; c) T. Nokami, T. Matsuo, Y. Inatomi, N. Hojo, T. Tsukagoshi, H. Yoshizawa, A. Shimizu, H. Kuramoto, K. Komae, H. Tsuyama, J. Yoshida, *J. Am. Chem. Soc.* **2012**, *134*, 19694 – 19700; d) T. Janoschka, M. D. Hager, U. S. Schubert, *Adv. Mater.* **2012**, *24*, 6397 – 6409; e) T. Suga, H. Ohshiro, S. Sugita, K. Oyaizu, H. Nishide, *Adv. Mater.* **2009**, *21*, 1627 – 1630.

[3] a) X.-P. Gao, H.-X. Yang, *Energy Environ. Sci.* **2010**, *3*, 174 – 189; b) Y. Liang, P. Zhang, S. Yang, Z. Tao, J. Chen, *Adv. Energy Mater.* **2013**, *3*, 600 – 605; c) Y. Liang, Z. Tao, J. Chen, *Adv. Energy Mater.* **2012**, *2*, 742 – 769.

[4] a) Z. Song, H. Zhou, *Energy Environ. Sci.* **2013**, *6*, 2280 – 2301; b) M. Zhou, J. Qian, X. Ai, H. Yang, *Adv. Mater.* **2011**, *23*, 4913 – 4917; c) Z. Song, H. Zhan, Y. Zhou, *Angew. Chem. Int. Ed.* **2010**, *49*, 8444 – 8448; *Angew. Chem.* **2010**, *122*, 8622 – 8626; d) H. Wu, S. A. Shevlin, Q. Meng, W. Guo, Y. Meng, K. Lu, Z. Wei, Z. Guo, *Adv. Mater.* **2014**, *26*, 3338 – 3343; e) B. Genorio, K. Pirnat, R. Cerc-Korosec, R. Dominko, M. Gaberscek, *Angew. Chem. Int. Ed.* **2010**, *49*, 7222 – 7224; *Angew. Chem.* **2010**, *122*, 7380 – 7382; f) K. Sakaushi, G. Nickerl, F. M. Wisser, D. Nishio-Hamane, E. Hosono, H. Zhou, S. Kaskel, J. Eckert, *Angew. Chem. Int. Ed.* **2012**, *51*, 7850 – 7854; *Angew. Chem.* **2012**, *124*, 7972 – 7976.

[5] a) X. Zhuang, F. Zhang, D. Wu, X. Feng, *Adv. Mater.* **2014**, *26*, 3081 – 3086; b) X. Zhuang, F. Zhang, D. Wu, N. Forler, H. Liang, M. Wagner, D. Gehrig, M. R. Hansen, F. Laquai, X. Feng, *Angew. Chem. Int. Ed.* **2013**, *52*, 9668 – 9672; *Angew. Chem.* **2013**, *125*, 9850 – 9854; c) D. Wu, F. Zhang, H. Liang, X. Feng, *Chem. Soc. Rev.* **2012**, *41*, 6160 – 6177; d) S. Li, D. Wu, C. Cheng, J. Wang, F. Zhang, Y. Su, X. Feng, *Angew. Chem. Int. Ed.* **2013**, *52*, 12105 – 12331; *Angew. Chem.* **2013**, *125*, 12327 – 12331.

[6] a) P. Kuhn, M. Antonietti, A. Thomas, *Angew. Chem. Int. Ed.* **2008**, *47*, 3450 – 3453; *Angew. Chem.* **2008**, *120*, 3499 – 3502; b) X. Liu, N. Fechler, M. Antonietti, *Chem. Soc. Rev.* **2013**, *42*, 8237 – 8265; c) P. Kuhn, A. Thomas, M. Antonietti, *Macromolecules* **2009**, *42*, 319 – 326; d) P. Kuhn, A. Forget, D. Su, A. Thomas, M. Antoniett, *J. Am. Chem. Soc.* **2008**, *130*, 13333 – 13337.

[7] C. Cao, X. Zhuang, Y. Su, Y. Zhang, F. Zhang, D. Wu, X. Feng, *Polym. Chem.* **2014**, *5*, 2057 – 2064.

[8] a) P. Kuhn, A. Forget, J. Hartmann, A. Thomas, M. Antonietti, *Adv. Mater.* **2009**, *21*, 897 – 901; b) M. J. Bojdys, J. Jeromenok, A. Thomas, M. Antonietti, *Adv. Mater.* **2010**, *22*, 2202 – 2205; c) K. Sakaushi, E. Hosono, G. Nickerl, T. Gemming, H. Zhou, S. Kaskel, J. Eckert, *Nat. Commun.* **2013**, *4*, 1485.

[9] a) L. Hao, B. Luo, X. Li, M. Jin, Y. Fang, Z. Tang, Y. Jia, M. Liang, A. Thomas, J. Yang, L. Zhi, *Energy Environ. Sci.* **2012**, *5*, 9747 – 9751; b) J. Wang, K. Pan, Q. He, B. Cao, *J. Hazard. Mater.* **2013**, *244 – 245*, 121 – 129; c) Z. Xiang, D. Cao, L. Huang, J. Shui, M. Wang, L. Dai, *Adv. Mater.* **2014**, *26*, 3315 – 3332.

[10] a) P. Novák, K. Müller, K. S. V. Santhanam, O. Haas, *Chem. Rev.* **1997**, *97*, 207 – 282; b) L. M. Zhu, A. W. Lei, Y. L. Cao, X. P. Ai, H. X. Yang, *Chem. Commun.* **2013**, *49*, 567 – 569.

[11] a) S. Laruelle, S. Grugeon, P. Poizot, M. Dollé, L. Dupont, J. M. Tarascon, *J. Electrochem. Soc.* **2002**, *149*, A627 – A634; b) D. Wang, J. Yang, X. Li, D. Geng, R. Li, M. Cai, T.-K. Sham, X. Sun, *Energy Environ. Sci.* **2013**, *6*, 2900 – 2906; c) J. Jamnik, J. Maier, *Phys. Chem. Chem. Phys.* **2003**, *5*, 5215 – 5220; d) Z. Wang, D. Luan, S. Madhavi, Y. Hu, X. W. Lou, *Energy Environ. Sci.* **2012**, *5*, 5252 – 5256; e) P. Simon, Y. Gogotsi, *Nat. Mater.* **2008**, *7*, 845 – 854.

[12] a) Z. Song, T. Xu, M. L. Gordin, Y. B. Jiang, I. T. Bae, Q. Xiao, H. Zhan, J. Liu, D. Wang, *Nano. Lett.* **2012**, *12*, 2205 – 2211; b) F. Xu, X. Chen, Z. Tang, D. Wu, R. Fu, D. Jiang, *Chem. Commun.* **2014**, *50*, 4788 – 4790; c) Y. Yang, C. Wang, B. Yue, S. Gambhir, C. O. Too, G. G. Wallace, *Adv. Energy Mater.* **2012**, *2*, 266 – 272; d) H. Wu, K. Wang, Y. Meng, K. Lu, Z. Wei, *J. Mater. Chem. A* **2013**, *1*, 6366 – 6372.

